Nuclear Inst, and Methods in Physics Research B 431 (2018) 47–54

Contents lists available at ScienceDirect

Nuclear Inst. and Methods in Physics Research B

journal homepage: www.elsevier.com/locate/nimb

High-resolution X-ray spectroscopy of highly charged tungsten EBIT plasma

S.C. Sanders[a,*], R. Silwal[a], B.H. Rudramadevi[a,b], A.C. Gall[a], E. Takacs[a]

[a] Department of Physics and Astronomy, Clemson University, Clemson, SC 29634, USA
[b] College of Science, Sri Venkateswara University, Tirupati, Andhra Pradesh 517502, India

ARTICLE INFO

Keywords:
Highly charged ions
EBIT
Tungsten
X-ray spectroscopy
EUV spectroscopy
Fusion research

ABSTRACT

Highly charged tungsten transitions can be used as a diagnostic tool for investigating performance of the fusion device. Systematic spectroscopic investigations of the radiative decay channels of the tungsten charge states allow for extending the fundamental understanding of highly charged ions and can serve as a diagnostic tool to improve applied plasma research. Electron beam ion traps (EBIT) offer the ability to generate emission from highly charged tungsten ions because of their charge state and excitation selectivity due to their quasi-mono-energetic electron beam. In this work, we report the current experimental capabilities of the EBIT at the National Institute of Standards and Technology (NIST). High-resolution measurements of EUV and x-ray transitions from tungsten charge states are shown, demonstrating our ability to produce and identify the spectral features of highly charged tungsten plasma. While the experimental results were limited by the lack of an absolute calibration of the spectrometer, we present approximate transition energies of two strong transitions from the Ti-like W^{52+} and Sc-like W^{53+} charge states. Our estimates agree quite well with the results of FAC simulations, where these strongest transitions were identified to originate from 3d-4f transitions. This decay channel has been shown to be the strongest transition for surrounding charge states.

1. Introduction

Spectroscopy of highly charged tungsten ions has garnered considerable interest due to its relevance in fusion plasma research. Tungsten has a considerable amount of favorable properties for being a primary plasma-facing material in fusion reactors, such as ITER and the ASDEX Upgrade tokamak devices. This provides impetus for understanding the properties of the various charge state distributions of highly charged tungsten plasma via accurate atomic data and spectral line identification measurements from spectroscopy experiments. This has been extensively discussed and highlighted by numerous research groups for over a decade in attempt to improve the current state of fusion reactors. An excellent review of these recent efforts was compiled by Kramida [1].

Erosion of tungsten into the fusion plasma is well documented, where the charge state distribution in the ITER plasma is expected to range from Ag-like W^{27+} at the outer edges of the plasma to F-like W^{65+} in the core of the plasma [2,3]. The core plasma of the ASDEX Upgrade device produces Kr-like W^{38+} to Ni-like W^{46+} ions, while lower charge states Sn-like W^{24+} to Rb-like W^{37+} are produced in the outer edge of the plasma [3]. Inevitably, tungsten ions will contaminate the fusion-plasma through interactions with the plasma, generating a wide range of tungsten ion charge states. Pütterich et al. (2008) compiled a comprehensive report on the effect of tungsten from experimental data from the ASDEX Upgrade, producing predictions for effects within the ITER plasma [3]. The presence of such tungsten charge states significantly enhances the power loss of the fusion-plasma device via emitted radiation, a serious issue that substantially degrades the performance of tokamaks [3]. The impurities due to tungsten can result in reductions in the fusion reactions that are required for energy production and potentially increasing the difficulty in confinement [3]. It is thus essential to understand the characteristics of highly charged tungsten plasma in order to develop a means for mitigating their effect on the fusion-plasma device [3].

Determining the tungsten charge state distribution within the fusion-plasma requires accurate atomic data (atomic transitions with identified wavelengths, transition intensities, ionization, excitation and recombination cross sections for many tungsten charge states) [4]. Many fusion-plasma devices utilize spectroscopic equipment to probe the fusion plasma to infer information about the plasma state. Observations of tungsten transitions from the fusion plasma can be and have been used to diagnose the state of the fusion device. For the anticipated ITER project, Peacock et al. (2007) provided theoretical estimates of x-ray and VUV spectroscopic data expected from the device along with outlining the various diagnostic instrumentation planned to help aide the reactor [2]. The core imaging x-ray spectrometer (CIXS)

* Corresponding author.
E-mail address: scsande@g.clemson.edu (S.C. Sanders).

https://doi.org/10.1016/j.nimb.2018.06.013
Received 13 October 2017; Received in revised form 7 June 2018; Accepted 13 June 2018
Available online 06 July 2018
0168-583X/

represents a crystal x-ray spectrometer experiment designed to diagnose the ITER plasma state, one of many diagnostic systems planned for the ITER project [5]. Such projects require fundamental laboratory measurements of spectral features of the various charge states of tungsten through spectroscopic line identification measurements. Spectroscopic observations of highly charged tungsten plasma produced in an electron beam ion trap (EBIT) help aide in fusion-plasma research (and general plasma research) as the EBIT can produce and confine nearly all tungsten charge states while offering charge state selectivity. Skinner (2008) provided a report on the importance of contributions from EBIT devices pertaining to improving fusion devices [6]. Such measurements of the highly charged extreme-ultraviolet tungsten spectra have been extensively studied and discussed [see for example, [7–11]].

Similarly, the EBIT has been used to measure transitions in the soft x-ray regime for a range of tungsten charge states, where we highlight a small sample of such observations related to the charge states of interest here [12–19]. An x-ray microcalorimeter was used to measure and identify energetic x-ray emissions for the Cu-like W^{45+} and Ni-like W^{46+} charge states providing accurate benchmarks for confirming the performance of dynamical plasma models and spectroscopic diagnostic tools of non-Maxwellian plasmas [13]. *M*-shell transitions, also recorded by an x-ray microcalorimeter array detector, were identified for the Zn-like W^{44+} through Co-like W^{47+} charge states [14]. Another measurement using a high-resolution crystal spectrometer reported identification of *M*-shell x-ray transitions of tungsten ions in the 5 Å–6 Å wavelength region from the Se-like W^{40+} to the Cr-like W^{50+} charge states, where the majority of the spectral lines were assigned to transitions from the 3d-4f and the 3p-4d shells [15]. Soft x-ray spectral features around 5.6 Å from Cu-like W^{45+} to Cr-like W^{50+} charge states were investigated in another measurement using a flat-crystal Bragg spectrometer, assigning the origin of these spectral lines to 3d-4f transitions [4]. A high-resolution grazing incidence spectrometer was used to observe 3s-3p and 3p-3d transitions between 19 Å and 24 Å arising from the K-like W^{55+} through Ne-like W^{64+} charge states [16]. This instrument also observed 3p-3p and 3p-3d transitions between 27 Å and 41 Å due to the *M*-shell tungsten ions from Al-like W^{61+} through Co-like W^{47+} [17]. *L*-shell x-ray transitions of Ne-like W^{64+} including few inner-shell collisional satellite lines arising from Mg-like W^{62+}, Na-like W^{63+}, F-like W^{65+}, and O-like W^{66+} charge states were recorded with a von-Hámos-type crystal spectrometer [18]. Dominate transitions from Si-like W^{60+} through Ne-like W^{64+} ions were also investigated with a crystal spectrometer in the 1.0 Å–1.6 Å wavelength region [4]. A detailed theoretical study aimed at providing accurate atomic data and theoretical spectra for comparison to the existing experimental data was performed for 10 tungsten charge states, from Ge-like W^{42+} through V-like W^{51+} [19]. This study identified the strongest transition to be consistently from a $3d_{3/2}$-$4f_{5/2}$ transition for all the ten charge states. They note that this particular transition from Ni-like W^{46+} to be very strong in their simulations, where the 3d-4f transition in all 10 tungsten spectra fall within a 300 eV region centered on the strong Ni-like W^{46+} feature. This interval should be well suited to infer the tungsten charge state balance in moderate-temperature tokamak plasmas [19]. These reports demonstrate the necessity of spectroscopic measurements of highly charged tungsten plasma as a means for diagnosing the plasma state of a fusion device, where all studies included comparisons to model simulations relevant to the particular experiment.

To our knowledge, measurements of the 3d-4f tungsten transitions have not been performed for the V-like W^{51+} through P-like W^{59+} charge states in the x-ray regime below 10 Å, representing one of the motivating factors of this work. In this report, we highlight our capability of producing high-resolution, x-ray observations of highly charged tungsten ions up to Sc-like W^{53+} as a means for line identification, allowing for further diagnosing the highly charged tungsten plasma, using the EBIT located at the National Institute of Standards and Technology (NIST). A high-resolution Johann-type curved crystal x-ray spectrometer was used to record the x-ray spectra [20]. Transitions in the EUV regime are also presented for validation and verification of the plasma species using a flat field EUV spectrometer, with additional broad-band x-ray spectra from a solid-state high-purity germanium (HPGe) x-ray detector for further corroboration [21].

The instruments used in this exploratory experiment are described in detail in Section 2. Section 3 outlines the experimental procedure used in the experiment. The results of the experiment are provided in Section 4, demonstrating the production of highly charged tungsten, the EUV spectra, and the high resolution x-ray spectra. The experimental high resolution x-ray spectra reported here were limited by the lack of an absolute reference for proper line identification. This report is aimed at demonstrating our current capabilities of producing proper spectroscopic measurements, in particular, those associated with x-ray transitions of highly charged tungsten ions. We were able to produce an approximate energy calibration to estimate the energy of the strongest 3d-4f transition of the tungsten charge states present in the EBIT, comparing these estimates to the predicted photon energies calculated by the Flexible Atomic Code (FAC) [22]. This is discussed in Section 5, where we also include the results of those in [19] to illustrate our capabilities as well as to provide additional spectroscopic tools for diagnosing hot plasmas.

2. Instrumentation

Highly charged tungsten ions were created and trapped using the NIST EBIT that consists of three main axially aligned components: the electron gun, the trapping region consisting of the drift tube electrodes, and the collector assembly [23]. Electrons forming the quasi-monoenergetic electron beam emanate from a Pierce-type electron gun, capable of producing a maximum electron beam current of 150 mA. Compression of the electron beam by an axial 3T magnetic field, produced by a pair of liquid-helium-cooled superconducting Helmholtz magnets, provides a minimum electron beam width of approximately 60 μm at the center of the trapping region.

The NIST EBIT is capable of producing electron beam energies from a few hundred eVs to 30 keV. The beam energy is controlled by a cylindrical shield electrode that surrounds the drift tube electrodes. The three drift tube electrodes located inside the shield electrode are electrically floated on top of the applied voltage to the shield electrode, where each drift tube electrode can be independently controlled to provide the proper axial trap potential for the ion species. The beam energy is proportional to the voltage applied to the trap electrodes and corrected for the space charge potential produced by the electron beam itself, which depends on the electron beam energy and current [24]. For this experiment, the space charge is on the order of a few hundred eV. The trapped ions are radially trapped by the axial magnetic field and also by the space charge produced by the electron beam.

Once exiting the drift tubes, the electron beam spreads out along the magnetic field lines and contacts the liquid-nitrogen-cooled collector. A metal vapor vacuum arc (MeVVA) ion source attached to the top of the EBIT chamber was used to generate singly charged tungsten ions that travel to the EBIT trapping region along the axial magnetic field lines [25].

The NIST EBIT has potential observation ports, allowing for simultaneous operation of the spectroscopic instruments. A flat-field variable-line-grating extreme ultraviolet spectrometer is currently attached to one of these observation ports [21]. This customized high-resolution spectrometer consists of a gold-coated spherical focusing mirror that images the radiation onto the entrance slit of the monochromator. A dispersive flat-field grazing-incidence reflection grating disperses the photons onto a liquid-nitrogen-cooled high spatial resolution charge-coupled device (CCD) camera sensitive to the energy of the EUV photons. Adjustment of the detector position allows for observations of wavelengths between approximately 1 nm–40 nm,

depending on the particular experiment.

A liquid-nitrogen-cooled high-purity germanium (HPGe) detector is installed on the NIST EBIT providing real-time broadband (approximately 1 keV–20 keV) measurements of x-ray emissions. The high count rate HPGe detector allows for fast optimization of the EBIT operating parameters. Monitoring the real time spectra allows for tuning of the electron beam energy, providing information about the plasma composition and charge states inside the EBIT to optimize the electron beam energies that produce strong resonant features.

High-resolution measurements in the x-ray regime are recorded with a Johann-type Bragg reflection curved-crystal x-ray spectrometer [20]. The lattice spacing of the crystal serves as the dispersive element, where the incident photons are Bragg reflected given the incident angle that satisfies the diffraction equation $n\lambda = 2\mathrm{dsin}(\theta)$,where d is the crystal lattice spacing, n is the order of diffraction of photons with wavelength λ, and θ represents the angle of incidence of the photon. The spectrometer is operated in vacuum to limit the absorption of x-ray photons within the spectrometer. A beryllium window separates the ultra-high vacuum of the EBIT from the spectrometer, attenuating the optical emissions from the EBIT plasma to prevent background light entering the CCD detector.

The spectrometer is designed such that the detector-crystal separation remains fixed with respect to the source, where a variable radius curved crystal mount is capable of cylindrically bending the crystal such that the detector remains on the Rowland focusing circle [26]. In general, it is easier experimentally to set the detector-crystal separation to establish a proper Rowland circle. The crystal mount then allows for a precise method for curving the crystal while under high vacuum to ensure the detector remains on the focusing circle. A model of the mechanical and vacuum components is presented in Fig. 1 (top), depicting the details of the geometry of the spectrometer. The two vacuum bellows represented in the figure are supported by the long arms of the rhombus, where one arm attaches to the detector and the other to the EBIT observation port (blue arrows). These arms are attached to the rotation stage (shown in green) with the variable radius crystal mounted to the opposing side of the rotation stage (red arrow). The crystal is located in the center of the rotation stage (tail of yellow arrow). Scanning of spectral features is performed by rotating the crystal by θ and the detector by 2θ with respect to the axis defined along the source-crystal separation. The rotation stage that supports the detector and crystal arms is thus a rhombus, where a linear encoder tracks the long diagonal of the rhombus while scanning to appropriately deduce the spectrometer angle θ. The detector must rotate at twice the spectrometer angle as to satisfy the condition that the detector remains on the Rowland circle whose diameter is equal to the radius of curvature of the crystal. Fig. 1 (bottom) illustrates the Rowland circle of the spectrometer geometry with respect the source of x-rays in the EBIT. The focusing circle radius is determined by the curvature of the crystal, where the Rowland circle radius is half the radius of curvature of the crystal. Photons originating from the EBIT source that satisfy the Bragg condition reflect off the crystal lattice, where meridional rays are directed towards the detector that lies tangent to the Rowland circle. As can be seen, photons with different wavelengths originating from the source correspond to different positions along the Rowland circle, where more energetic photons are observed at smaller Bragg angles. We note that the components represented in the figure are not drawn to scale, especially the source.

A CCD detector with 2048 × 2048 pixels with a pixel width of 13.6 μm was used, providing an active detection area of high spatial resolution. The active area of the CCD chip is back-illuminated to allow for direct detection of these soft x-ray photons with high quantum efficiency and low readout noise. Thermoelectric cooling of the detector to −75 °C produces negligible thermal noise.

The accessible x-ray energy range of the spectrometer is due in part to the mechanical limitations of the spectrometer as well as the lattice spacing of the crystal used. We note that the plane of dispersion of the crystal for this high-resolution spectrometer is perpendicular to the electron beam axis, such that the dispersive plane of the crystal is along the short axis of the EBIT plasma.

Calibration of the high-resolution spectrometer requires observations of known reference lines in the photon energy range of interest. This allows for determining the dispersion relation of the detector for accurate identification of the observed spectral lines. Calibration elements that produce known reference lines within the detector energy bandwidth can be introduced into the EBIT plasma. Alternatively, a standard emission source aligned with the slits of the EBIT drift tube can be used to calibrate the high-resolution instrument.

Recently, an additional nearly identical high-resolution spectrometer has been installed onto the NIST EBIT. This spectrometer is oriented such that the plane of dispersion of its dispersive element is parallel to the electron beam, providing the capability of simultaneous high resolution polarization measurements in the x-ray regime. Dual high-resolution Johann-type crystal x-ray spectrometers equipped with proportional counter detectors have been successfully used in the past for high precision tests of quantum electrodynamics [27] and x-ray polarization experiments [28] at the NIST EBIT facility. These measurements required considerable run times and expensive operational costs, mainly due to the efficiency of the detectors used. The inclusion of the CCD cameras greatly improves the efficiency and sensitivity of these spectrometers. With both high-resolution spectrometers operational, simultaneous observations enhance our experimental capabilities, such as measuring the polarization of the highly charged tungsten x-ray transitions. This twin instrument was assembled and tested at Clemson University. At the time of the experiment, the second spectrometer was in the process of being tested on the NIST EBIT and shall be operational soon. Such experimental capabilities of simultaneous orthogonal spectroscopic observations is further bolstered by the work of Beiersdorfer et al. (2016), where a spectrometer has been designed and tested on the LLNL EBIT that utilizes two spherically bent crystals. This novel instrument has a high resolving power, capable of observing x-ray emissions parallel or perpendicular to the electron beam for polarization and imaging purposes, or can focus photons in both observation planes to a singular detector position for an enhanced signal-to-noise ratio [29].

Fig. 2(a) and (b) show the two high-resolution instruments installed on opposite ports of the NIST EBIT as well as the flat field EUV spectrometer and broad-band HPGe x-ray spectrometer. The MeVVA is indicated in Fig. 2(a). This photograph illustrates how the spectrometers are attached to the EBIT for simultaneous operation and demonstrates the orientation of the instruments.

3. Experimental methods

To create the V-like W^{51+}, Ti-like W^{52+} and Sc-like W^{53+} charge states during the experiment, the electron beam energy must be tuned such that it overcomes the ionization potential of the charge state. The respective ionization potentials are 4.71 keV, 4.93 keV, and 5.06 keV [16]. Thus, the EBIT was operated at shield voltages between 5.2 kV and 5.5 kV and at beam currents of approximately 140 mA. The x-ray spectrometers had collection times of three minutes per observation. The EUV spectrometer integrated five, one minute exposures per observation. Each instrument collected six spectra for each measurement. This resulted in a nominal total acquisition time of 18 min and 30 min for the x-ray and EUV spectrometers, respectively.

A Si (111) crystal served as the dispersing element in the high-resolution spectrometer, producing an observable energy range of 2.22 keV–4.59 keV due to the crystal lattice spacing of 2d = 6.271 Å. The high-resolution spectrometer was set to Bragg angles that correspond to the strongest expected 3d-4f transitions of the V-like W^{51+}, Ti-like W^{52+} and Sc-like W^{53+} charge states. These angles were 53.51°, 52.74°, and 52.00° and are indicative of the central detector energy via the Bragg diffraction equation and the detector energy bandwidth at

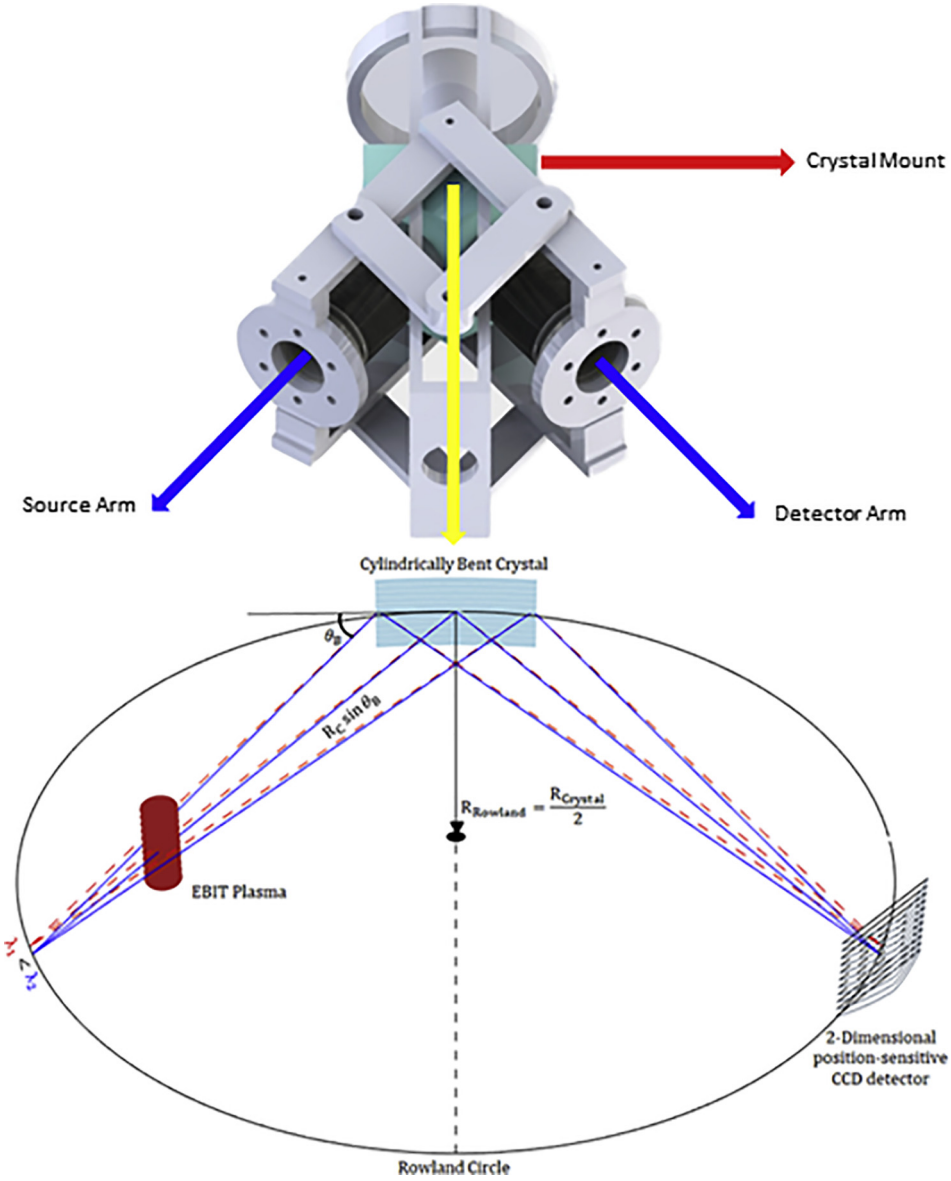

Fig. 1. (top) A model of the spectrometer body showing the mechanical and vacuum components. The two vacuum bellows represent the detector and source arms (blue arrows). These arms are attached to the rotation stage (shown in green). The crystal mount is mounted to the opposing side of the rotation stage (red arrow), where the crystal is located inside of the stage (tail of yellow arrow). The rhombic arms are visible, demonstrating how the rotation stage and detector arm rotate at θ and 2θ, respectively. (bottom) A schematic drawing of the Johann-type crystal spectrometer used in the experiment. This figure demonstrates the curvature of the crystal, which defines the radius of the focusing circle. The associated source and 2-Dimensional position-sensitive detector are shown. The source is located inside of the Rowland circle to increase the spectral bandpass as well as the intensity. The schematic demonstrates how different wavelengths of the transitions correspond to different positions along the Rowland circle due to the Bragg condition. We note that this schematic is not drawn to scale and the components are enlarged for clarity.

that particular spectrometer setting. The assumed central detector energies were approximately 2.46 keV, 2.48 keV, and 2.51 keV, respectively. The spectrometer was scanned such that transitions from different charge states of tungsten could be observed simultaneously within the nominal detector bandwidth of 100 eV.

4. Results

Spectra from all three instruments were recorded for each measurement. The HPGe spectra clearly indicated a strong presence of photons with energies in the 2 keV–3 keV range. An example spectrum measured during the experiment is shown in Fig. 3. Fig. 3(b) represents the tungsten spectrum from charge states produced by the EBIT at a beam energy of 5.3 keV and a beam current of 140 mA, where tungsten was injected into the EBIT by the MeVVA. Fig. 3(a) represents a measured spectrum of the EBIT plasma with the same electron beam parameters but without the injection of tungsten ions into the EBIT by the MeVVA, representing the EBIT background spectrum. It is clear that strong tungsten transitions occur within the soft x-ray regime of interest when there is an injection of tungsten ions into the EBIT by the MeVVA. These photon energies are mostly within the observable energy range of the high-resolution crystal spectrometer.

Simultaneous collection of the EUV spectra aids in the optimization of the signal as well as providing information about the EBIT plasma charge state distribution. Well-known EUV spectra exists for the *M*-shell ions of tungsten [9], in particular for the Cr-like W^{50+}, V-like W^{51+}, Ti-like W^{52+}, and Sc-like W^{53+} charge states. A comparison of our measured EUV spectra with their reported EUV spectral lines verifies that these high charge states of tungsten are being produced in the EBIT. Fig. 4 represents the three EUV spectra in the 12.0 nm–15.5 nm wavelength range at beam energies of 5.4 keV [Fig. 4(a)], 5.3 keV [Fig. 4(b)], 5.2 keV [Fig. 4(c)]. Several of the observed spectral features were identified in a previous measurement at the NIST EBIT using the same EUV spectrometer [9], confirming the existence of the desired charge states of tungsten.

The high-resolution spectrometer measured x-ray spectra with high count rates at various Bragg angles and beam energies. Fig. 5 shows the uncalibrated high-resolution soft x-ray tungsten one-dimensional spectra at two different Bragg angles and at the same beam energy of 5.3 keV. Fig. 5(a) represents the measured spectrum for a Bragg angle of 53.51°. At this spectrometer angle the spectrum includes of photons in the 2.4 keV–2.5 keV range. An intense tungsten transition was recorded by the detector around channel number 750. Two less intense tungsten spectral lines were observed around channel numbers 625 and 1100.

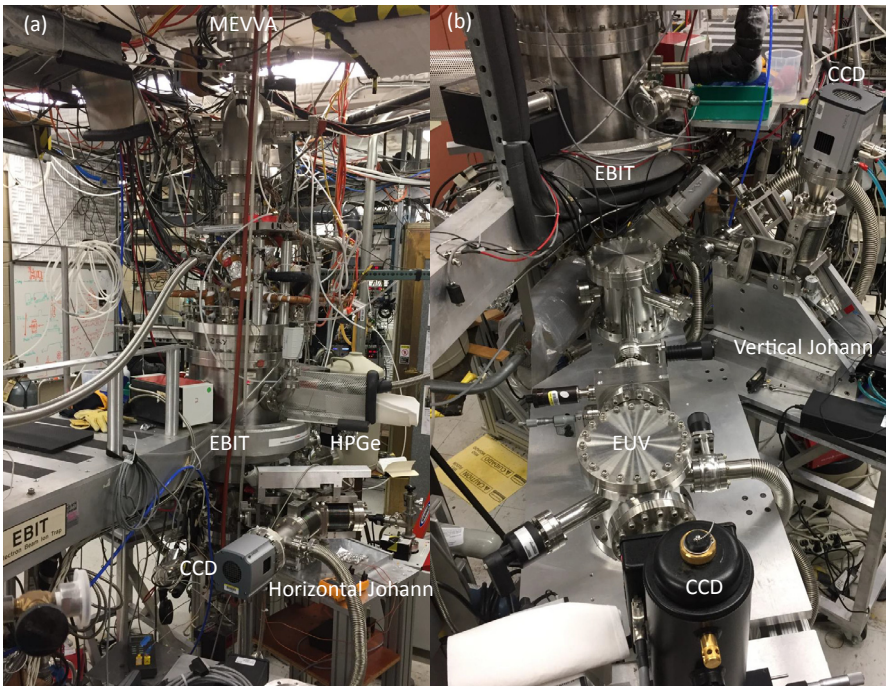

Fig. 2. The NIST EBIT and the attached instruments. The electron beam axis is vertical. (a) The high-resolution x-ray spectrometer (oriented perpendicular to the electron beam, labeled as "Horizontal Johann") and the HPGe solid state detector attached to two of the EBIT observation ports. (b) The second, recently installed high-resolution x-ray spectrometer (oriented parallel to the electron beam, labeled as "Vertical Johann") and the flat-field EUV instrument attached to two additional EBIT observation ports.

Fig. 5 (b) represents the measured spectrum for a Bragg angle of 52.74°. The photon energy bandwidth is nearly the same as in Fig. 5(a), except that the spectrum is shifted towards higher energies by about 25 eV. Two clear tungsten transitions are evident around channel numbers 1275 and 1675.

These spectra indicate our ability to produce high-resolution soft x-ray tungsten spectra with good statistics. The spectrometer registered higher energy spectral features when it was scanned to record higher energies confirming the energy scanning capability of the spectrometer.

It is accepted that higher charge states of an ion species produce more energetic transitions. Using the HPGe detector as well as the EUV spectrometer, we have confirmed the production of various charge states of tungsten. Given that the charge state distribution is determined by the EBIT electron beam energy, the higher charge states of tungsten become more dominant in the EBIT plasma with increasing energy. Furthermore, as higher charge states are produced, the intensity of the corresponding spectral features increases, while the intensity of the transitions produced from lower charge states decreases.

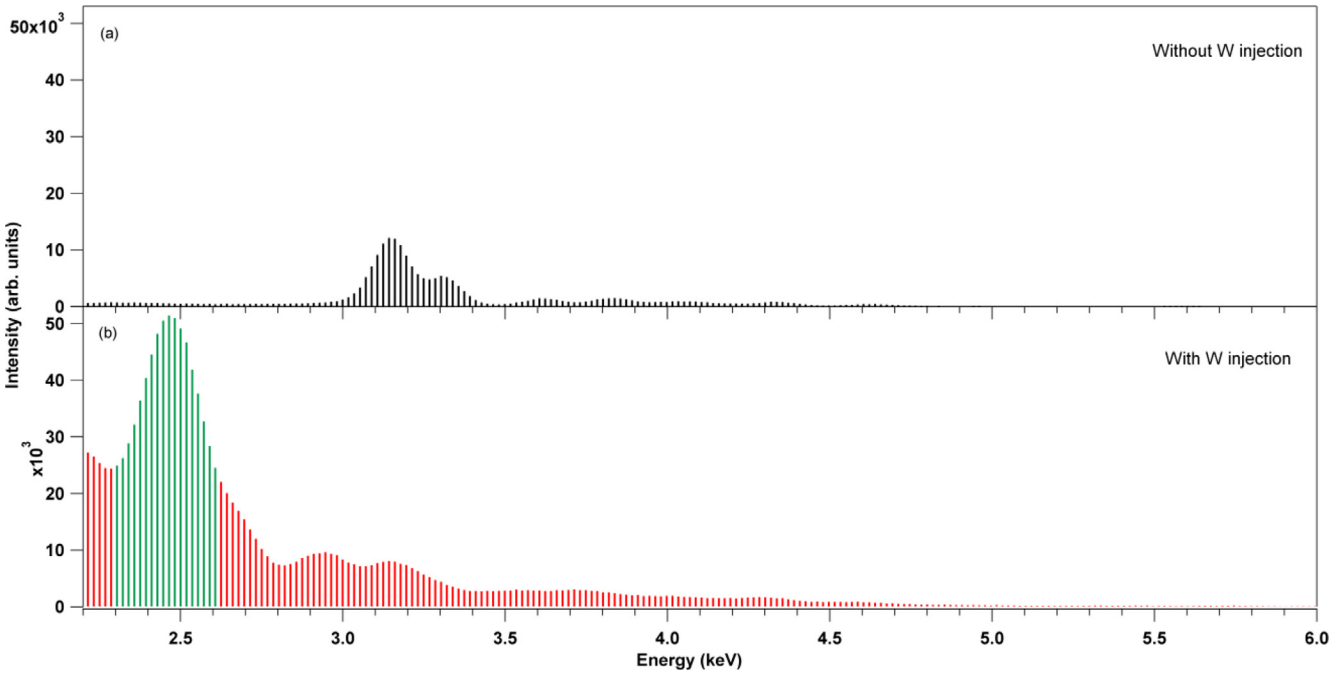

Fig. 3. HPGe detector broad-band x-ray spectrum of the EBIT plasma at an electron beam energy of 5.3 keV and beam current of 140 mA with the injection of tungsten ions into the EBIT by the MeVVA (b) and without the injection of tungsten, representing the background spectrum of the EBIT plasma (a). Both spectra were recorded over a three minute integration time. The highlighted energy region in (b) represents the spectral range of interest.

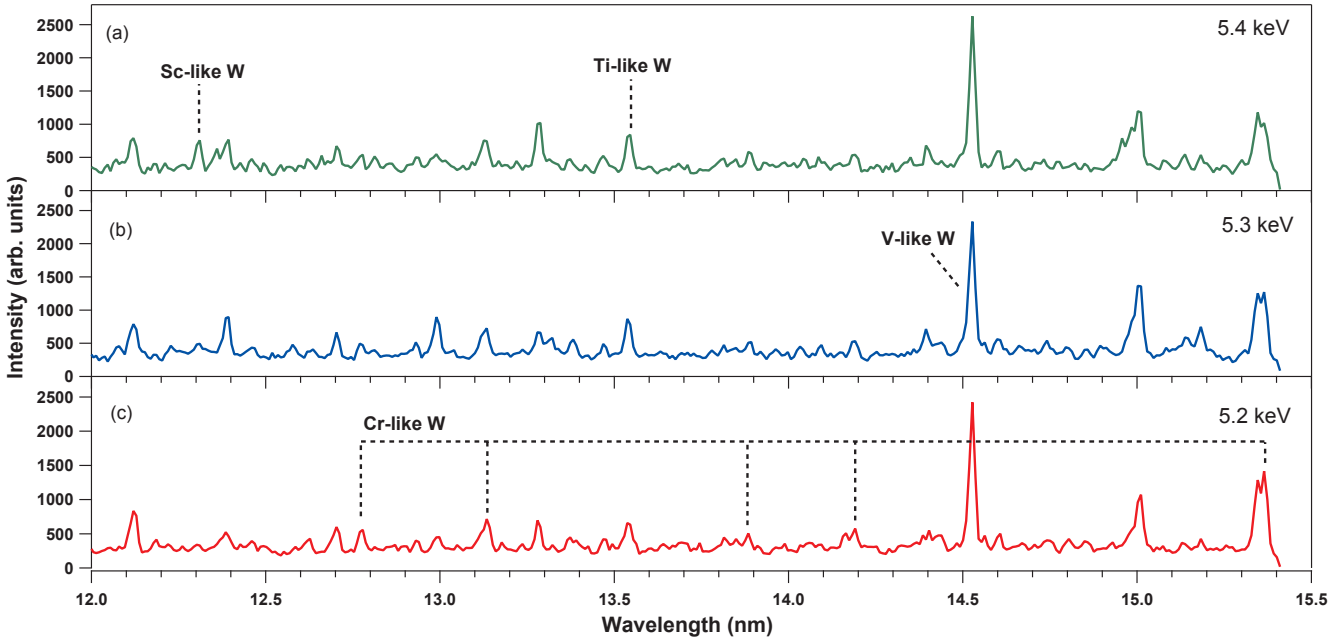

Fig. 4. Observed EUV spectra in the wavelength region of 12.0 nm through 15.5 nm at the beam energies of 5.4 keV (a), 5.3 keV (b) and 5.2 keV (c). Certain identified spectral lines are noted that correspond to the results of [5] providing verification of the tungsten charge states produced.

Generally, the photon energy of the transitions (such as the 3d-4f transitions of tungsten) increase with charge state. Fig. 6 provides evidence of this conclusion. Fig. 6 represents four tungsten spectra at four different beam energies of 5.5 keV (a), 5.4 keV (b), 5.3 keV (c), and 5.2 keV (d), all recorded at the same spectrometer setting of 52.74°. The positions of the spectral features are the same as those in Fig. 5(b). As the beam energy is increased, the intensity of the observed spectral features in Fig. 6 is clearly enhanced, where the decrease in the spectrometer setting to 52.74° from 53.51° implies the detector energy bandwidth is shifted to detect the more energetic photons from the higher charge states by approximately 25 eV. The intensities of all spectra were normalized to the total integration time. At the time of the experiment, a proper calibration source in the photon energy range of interest was not observed. This prevented an absolute calibration of the spectra and prevents us from confidently identifying the spectral features with reasonable uncertainty. We were able to generate a relative, approximate photon energy calibration, the results of which are discussed in Section 5.

5. Discussions

To our knowledge, there are no published spectral line identifications of the V-like W^{51+} to P-like W^{59+} charge states in the x-ray regime below 10 Å. Identifying these *M*-shell transitions of highly charged tungsten provides an enhanced fundamental understanding of highly charged tungsten plasma. Spectroscopic measurements aid applied plasma research, in particular, fusion devices employing tungsten shielding as the interior confinement body. Leaching of tungsten into the fusion plasma produces many tungsten charge states that negatively affect the performance of the tokamak. The tungsten impurities

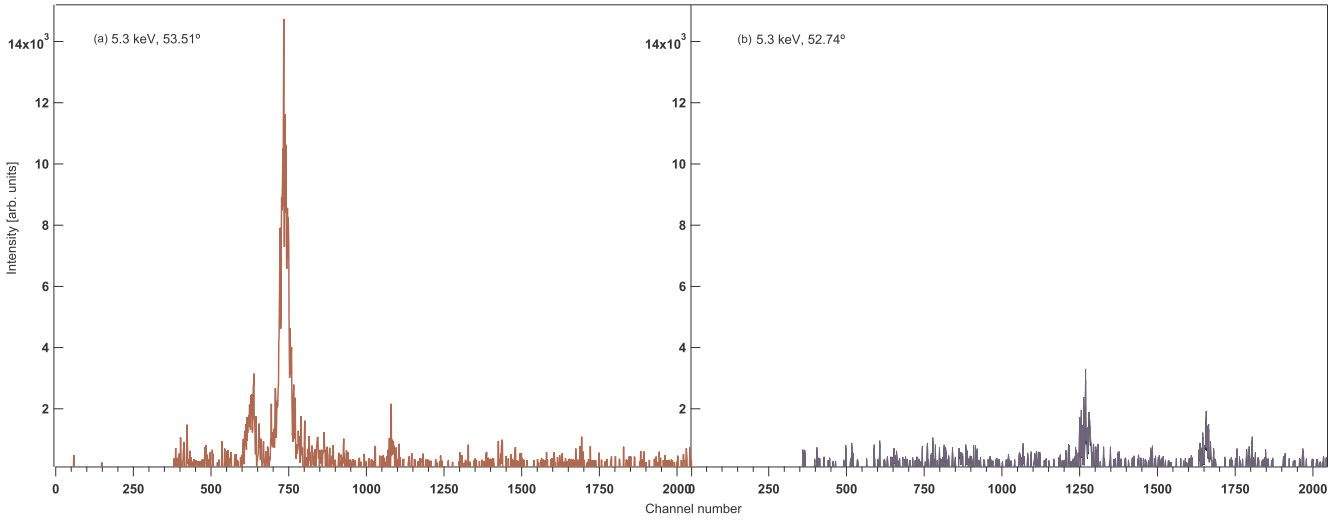

Fig. 5. Uncalibrated, high resolution, soft x-ray tungsten spectra at two different Bragg angles at an electron beam energy of 5.3 keV. This clearly demonstrates our capability of producing high resolution x-ray measurements.

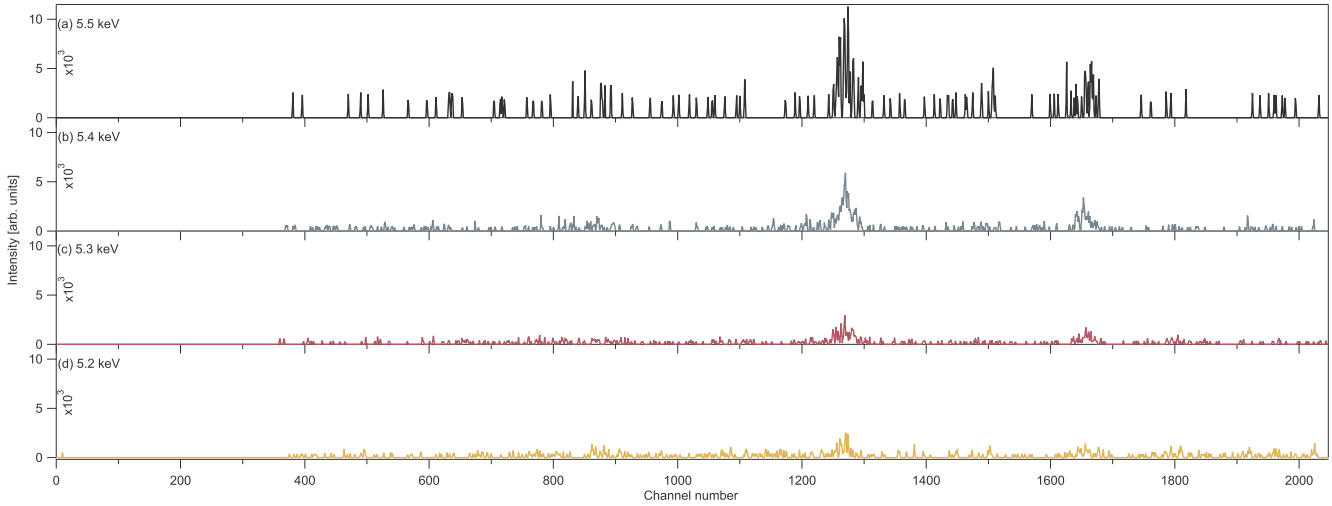

Fig. 6. Four uncalibrated tungsten x-ray spectra at three different beam energies at a Bragg angle of 52.74°. The relative intensity of the spectral features of the higher charge states of tungsten is dependent on the electron beam energy. The intensities of each spectrum were normalized to the total integration time.

eventually de-excite through numerous processes, where some undergo radiative decay. These transitions and the tungsten charge state distribution affect the fusion-plasma devices in many ways, as they can alter the fusion-plasma state. To understand and quantify the effect of highly charged tungsten plasma and the associated transitions requires accurate identification of the spectral features. Establishing the link between tungsten transitions and the associated charge state then allows for producing estimates of the charge state distribution of the tungsten plasma (a common practice in plasma research), through which a more complete description of the plasma state and how it evolves can be produced. Therefore, we emphasize the importance of a more complete description of the highly ionized tungsten spectra as it provides a means for improving fusion-plasma devices. The high resolution, x-ray spectrometer is thus an integral part in diagnosing fusion-plasma research.

We were able to produce a relative energy calibration of the observed high-resolution x-ray spectra, allowing for an estimation of the spectral line energy. This approximate calibration of the spectra was performed by scanning a pair of spectral lines across the detector. The scan was performed over an approximate energy shift of 25 eV, where the spectrometer angle was changed such that the central energy of the detector increased by the assumed energy shift while maintaining the same EBIT operating parameters. The use of the linear encoder to determine the spectrometer setting provides a fair estimate of the central energy but this is not an absolute reference. The relative shift in the centroid position of the spectral line due to the assumed energy shift of approximately 25 eV allowed for an estimation of the detector dispersion relation, producing the relative, approximate photon energy calibration.

We preliminarily assigned the strongest spectral features to photon energies of approximately 2450 eV and 2508 eV for the Ti-like W^{52+} and Sc-like W^{53+} charge states, respectively. Our assignment of these energy values is crude given our calibration method. The results of FAC simulations for these charge states aided our transition energy assignments, where considerable agreement is clear between the two results. Furthermore, the FAC results consistently established the 3d-4f transitions of the Ti-like W^{52+} and Sc-like W^{53+} charge states to be the strongest spectral features [22]. This conclusion is bolstered by the results of [19]. Applying the results of our experiment here with those of [19], we determined the dependence of the photon energy of the strongest 3d-4f transitions as a function of the tungsten charge state. Fig. 7 demonstrates this dependence. From our approximate energy

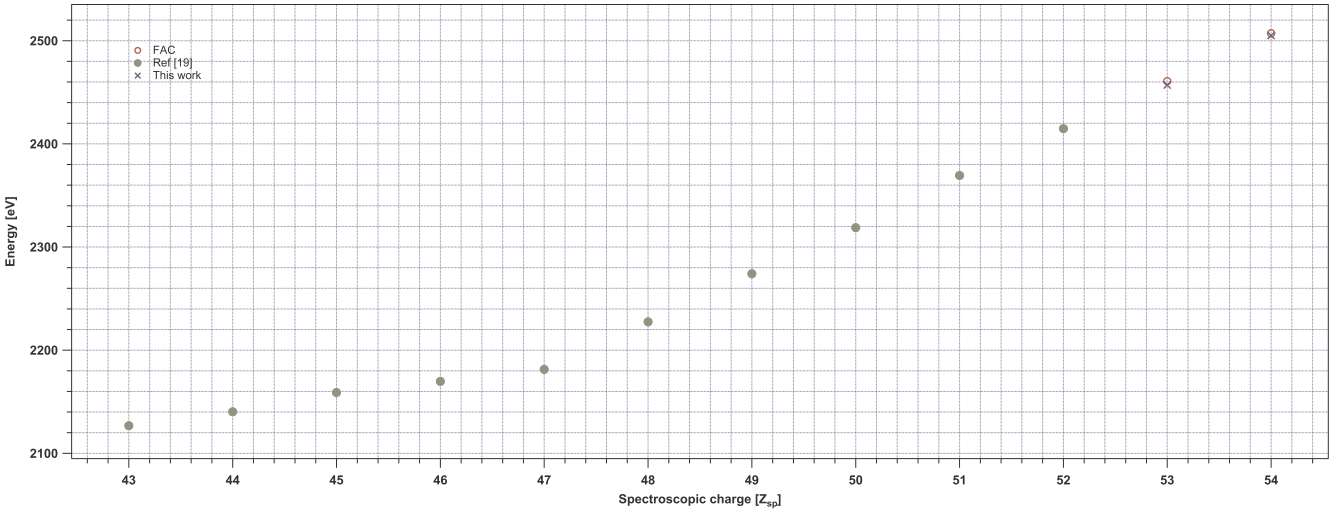

Fig. 7. Estimated transition energies of the strongest 3d-4f transition produced by the Ge-like W^{42+} through V-like W^{51+} charge states [19] and the FAC results of the same strong 3d-4f transition for the Ti-like W^{52+} and Sc-like W^{53+} charge states. Our estimated photon energy for the strong 3d-4f transition from the Ti-like W^{52+} and Sc-like W^{53+} charge states is shown. These results follow the apparent trend modeled by [22] and agree quite well with the FAC calculations.

calibration, the strongest transitions we observed, shown in Fig. 5, follow the modeled trend by [19] and agree quite well with the results of the FAC calculation for the Ti-like W^{52+} and Sc-like W^{53+} charge states. We note that the spectral features we observed were well isolated or dominate relative to other features in the spectra, where these spectral lines could provide reliable diagnostic information about the charge state balance of tokamak plasmas.

6. Conclusions and future works

We have illustrated our ability to produce high-resolution soft x-ray spectra with high sensitivity from highly charged tungsten plasma produced by the NIST EBIT. The lack of a known reference line in this photon energy regime prevented an absolute wavelength calibration. Through our approximate calibration, our preliminary results agree quite well with the current modeled calculations. This provides additional motivation to extend our high resolution measurements of the V-like W^{51+} through P-like W^{59+} charge states in the x-ray regime given the capability of the NIST EBIT to produce these charge states of tungsten by increasing electron beam energy. Future experiments will be performed with the inclusion of a known reference wavelength for accurate line identifications. These spectroscopic measurements will identify tungsten transitions from the charge states of interest, providing an invaluable diagnostic tool for fusion-plasma devices.

The inclusion of the second high-resolution spectrometer will allow for polarization measurements of the tungsten emissions for determining the magnetic sublevel populations of the species. These polarization measurements will improve our understanding of the atomic processes occurring inside of the plasma. For instance, quantifying the polarization of the photon field allows for improving the non-Maxwellian collisional radiative code (NOMAD) developed to simulate the EBIT plasma that currently does not calculate the effect of photon polarization in the x-ray region [30]. Such modeling efforts of plasma dynamics enhance our understanding of how the plasma state evolves. In particular, the effect of polarized x-ray emissions within magnetically-confined plasma is not well understood. Simultaneous operation of both spectrometers could help illuminate such effects. Polarization measurements of x-ray emissions have been performed on confined plasmas, allowing for diagnostic studies of plasma parameters such as the directionality of non-Maxellian electron currents [31,32]. Our capability of investigating these effects within highly charged tungsten plasma is motivated by such efforts.

Acknowledgements

This work was supported in part by the NIST Grant # 70NANB16H204. The authors wish to acknowledge the NIST Atomic Spectroscopy Group for the use of the EBIT. The authors would also like to acknowledge Yu. Ralchenko of NIST for his theoretical calculations, J.D. Gillaspy of NSF for his experimental contribution, and A. Henins, C. Szabo, and L.T. Hudson of NIST for their support and effort in connection with the high-resolution spectrometers.

References

[1] A. Kramida, Can. J. Phys. 89 (2011).
[2] N.J. Peacock, M.G. O'Mullane, R. Barnsley, M. Tarbutt, Can. J. Phys. 86 (2007) 277–284.
[3] T. Pütterich, R. Neu, R. Dux, A.D. Whiteford, M.G. O'Mullanethe ASDEX Upgrade Team, Plasma Phys. Control. Fusion 50 (2008) 085016.
[4] C. Biedermann, R. Radtke, R. Seidel, T. Pütterich, Phys. Scr. T134 (2009) 014026.
[5] P. Beiersdorfer, J. Clementson, J. Dunn, M.F. Gu, K. Morris, Y. Polpady, E. Wang, M. Bitter, R. Feder, K.W. Hill, D. Johnson, R. Barnsley, J. Phys. B: At. Mol. Opt. Phys. 43 (2010) 144008.
[6] C.H. Skinner, Can. J. Phys. 86 (2008) 285–290.
[7] Yu. Ralchenko, J. Reader, J.M. Pomeroy, J.N. Tan, J.D. Gillaspy, J. Phys. B: At. Mol. Opt. Phys. 40 (2007) 3861–3875.
[8] Yu Ralchenko, I.N. Draganic, J.N. Tan, J.D. Gillaspy, J.M. Pomeroy, J. Reader, U. Feldman, G.E. Holland, J. Phys. B: At. Mol. Opt. Phys. 41 (2008) 021003.
[9] Yu. Ralchenko, I.N. Draganic, D. Osin, J.D. Gillaspy, J. Reader, Phys. Rev. A 83 (2011) 032517.
[10] Yu. Ralchenko, J.D. Gillaspy, J. Reader, D. Osin, J.J. Curry, Y.A. Podpaly, Phys. Scr. T156 (2013) 014082.
[11] A. Kramida, Yu. Ralchenko, J. Reader, NIST ASD Team, NIST Atomic Spectra Database (version 5.4), 2016, Available from: http://physics.nist.gov/asd.
[12] J.D. Gillaspy, I.N. Draganić, Yu. Ralchenko, J. Reader, J.N. Tan, J.M. Pomeroy, S.M. Brewer, Phys. Rev. A 80 (2009) 010501(R).
[13] Yu. Ralchenko, J.N. Tan, J.D. Gillaspy, J.M. Pomeroy, E. Silver, Phys. Rev. A 74 (2006) 042514.
[14] J. Clementson, P. Beiersdorfer, G.V. Brown, M.F. Gu, Phys. Scr. 81 (2010) 015301.
[15] P. Neill, C. Harris, A.S. Safronova, S. Hamasha, S. Hansen, U.I. Safronova, P.Can. Beiersdorfer, J. Phys. 82 (2004).
[16] J. Clemsentson, P. Beiersdorfer, Phys. Rev. A 81 (2010) 052059.
[17] T. Lennartsson, J. Clementson, P. Beiersdorfer, Phys. Rev. A 87 (6) (2015) 062505.
[18] P. Beiersdorfer, J.K. Lepson, M.B. Schneider, M.P. Bode, Phys. Rev. A 86 (2012) 012509.
[19] J. Clementson, P. Beiersdorfer, T. Brage, M.F. Gu, At. Data Nucl. Data Tables 100 (2014) 577–649.
[20] H.H. Johann, Z. Phys. 69 (1931) 185.
[21] B. Blagojevic, E.-O. Le Bigot, K. Fahy, A. Aguilar, K. Makonyi, E. Takács, J.N. Tan, J.M. Pomeroy, J.H. Burnett, J.D. Gillaspy, J.R. Roberts, Rev. Sci. Instrum. 76 (2005) 083102.
[22] M.F. Gu, Can. J. Phys. 86 (2008) 675–689.
[23] J.D. Gillaspy, Phys. Scr. T71 (1997) 99.
[24] J.V. Porto, I. Kink, J.D. Gillaspy, Rev. Sci. Instrum. 71 (2000) 3050.
[25] G.E. Holland, C.N. Boyer, J.F. Seely, J.N. Tan, J.M. Pomeroy, J.D. Gillaspy, Rev Sci Instrum. 76 (2005) 073304.
[26] A. Henins, Rev. Sci. Instrum. 58 (1987).
[27] C.T. Chantler, M.N. Kinnane, J.D. Gillaspy, L.T. Hudson, A.T. Payne, L.F. Smale, A. Henins, J.M. Pomeroy, J.N. Tan, J.A. Kimpton, E. Takacs, K. Makonyi, Phys. Rev. Lett. 109 (2012) 153001.
[28] E. Takács, E.S. Meyer, J.D. Gillaspy, J.R. Roberts, C.T. Chantler, L.T. Hudson, R.D. Deslattes, C.M. Brown, L.M. Laming, U. Feldman, J. Dubau, M.K. Inal, Phys. Rev. A 54 (1996) 1342.
[29] P. Beiersdorfer, E.W. Magee, N. Hell, G.V. Brown, Rev. Sci. Instrum. 87 (2016) 11E339.
[30] Yu. Ralchenko, Y. Maron, J. Quant. Spectrosc. Radiat. Transfer 71 (2001) 609–621.
[31] R. Beier, C. Bachmann, R. Burhenn, J. Phys. D: Appl. Phys. 14 (1981) 643–648.
[32] H. Nishimura, Y. Inubushi, M. Ochiai, T. Kai, T. Kawamura, S. Fujioka, M. Hashida, S. Simizu, S. Sakabe, R. Kodama, K.A. Tanaka, S. Kato, F. Koike, S. Nakazaki, H. Nagatomo, T. Johzaki, K. Mima, Plasma Phys. Control. Fusion 47 (2005) B823–B831.